


Aftershock Spatiotemporal Activity and Coseismic Slip Model of the 2022 Mw 6.7 Luding Earthquake: Fault Geometry Structures and Complex Rupture Characteristics

Qibo Hu ^{1,2}, Hongwei Liang ^{1,3}, Hongyi Li ², Xinjian Shan ¹ and Guohong Zhang ^{1,3,4,*} 

¹ State Key Laboratory of Earthquake Dynamics, Institute of Geology, China Earthquake Administration, Beijing 100029, China; huqibo@ies.ac.cn (Q.H.); lianghw@ies.ac.cn (H.L.); xjshan@ies.ac.cn (X.S.)

² Key Laboratory of Intraplate Volcanoes and Earthquakes, China University of Geosciences (Beijing), Ministry of Education, Beijing 100083, China; lih@cugb.edu.cn

³ Institute of Disaster Prevention, No. 465, Xueyuan Street, Yanjiao High Tech Zone, Sanhe 065201, China

⁴ Urumqi Institute of Central Asia Earthquake, China Earthquake Administration, Urumqi 830011, China

* Correspondence: zhanggh@ies.ac.cn

Abstract: On 5 September 2022, the moment magnitude (Mw) 6.7 Luding earthquake struck in the Xianshuihe Fault system on the eastern edge of the Tibet Plateau, illuminating the seismic gap in the Moxi segment. The fault system geometry and rupture process of this earthquake are relatively complex. To better understand the underlying driving mechanisms, this study first uses the Interferometric Synthetic Aperture Radar (InSAR) technique to obtain static surface displacements, which are then combined with Global Positioning System (GPS) data to invert the coseismic slip distribution. A machine learning approach is applied to extract a high-quality aftershock catalog from the original seismic waveform data, enabling the analysis of the spatiotemporal characteristics of aftershock activity. The catalog is subsequently used for fault fitting to determine a reliable fault geometry. The coseismic slip is dominated by left-lateral strike-slip motion, distributed within a depth range of 0–15 km, with a maximum fault slip > 2 m. The relocated catalog contains 15,571 events. Aftershock activity is divided into four main seismic clusters, with two smaller clusters located to the north and south and four interval zones in between. The geometry of the five faults is fitted, revealing the complexity of the Xianshuihe Fault system. Additionally, the Luding earthquake did not fully rupture the Moxi segment. The unruptured areas to the north of the mainshock, as well as regions to the south near the Anninghe Fault, pose a potential seismic hazard.



Academic Editors: Zhangfeng Ma, Jihong Liu and Yosuke Aoki

Received: 28 November 2024

Revised: 22 December 2024

Accepted: 26 December 2024

Published: 28 December 2024

Citation: Hu, Q.; Liang, H.; Li, H.; Shan, X.; Zhang, G. Aftershock Spatiotemporal Activity and Coseismic Slip Model of the 2022 Mw 6.7 Luding Earthquake: Fault Geometry Structures and Complex Rupture Characteristics. *Remote Sens.* **2025**, *17*, 70. <https://doi.org/10.3390/rs17010070>

Copyright: © 2024 by the authors. Licensee MDPI, Basel, Switzerland. This article is an open access article distributed under the terms and conditions of the Creative Commons Attribution (CC BY) license (<https://creativecommons.org/licenses/by/4.0/>).

Keywords: 2022 Luding earthquake; Xianshuihe Fault; InSAR; machine learning; earthquake detection and location

1. Introduction

The Xianshuihe Fault zone (XSF) is located in the southeast of the Tibet Plateau, with a total length of approximately 400 km. The orientation is from northwest to southeast, separating the Sichuan–Yunnan block from the Bayan Har block [1]. It is a large left-lateral strike-slip fault zone. Since 1700, at least 16 $M > 6.5$ earthquakes have occurred along this fault zone, including 8 $M > 7.0$ earthquakes (Figure 1a). They have ruptured almost the entire XSF [1,2]. Geological and geodetic studies have shown that the XSF has a slip rate of 10 ± 5 mm/yr [3–6], which is faster than that of the Ganzi–Yushu Fault zone to the west. It is a concentrated zone of tectonic deformation and strong seismic activity, but there have been no major earthquakes in the past 40 years, especially in the southern

XSF, the Moxi section. Since the 1786 M7.75 Kangding earthquake, there have been no $M > 6.5$ earthquakes, and it is considered a seismic gap [7–9].

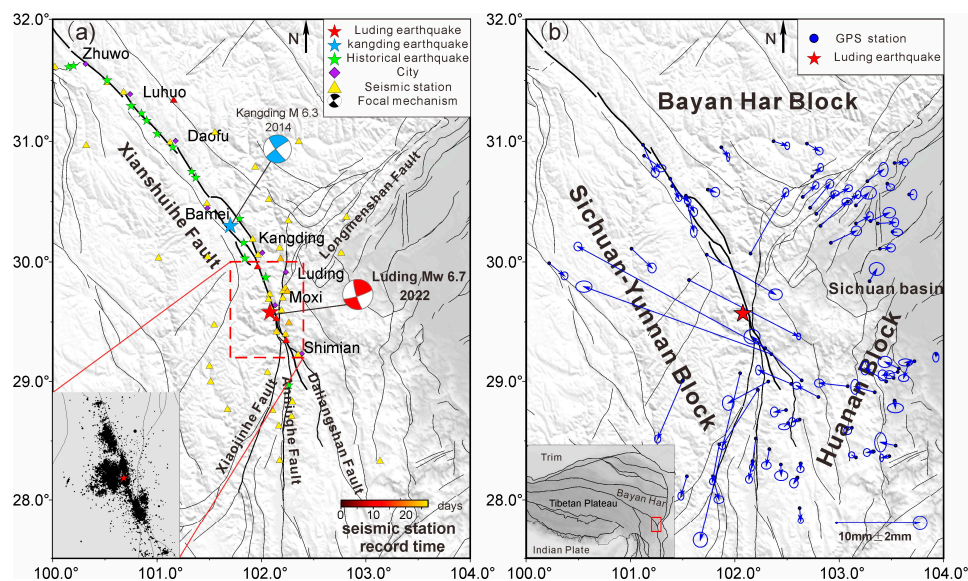


Figure 1. Tectonic map of the Luding earthquake region. (a) The red star marks the mainshock epicenter in Luding, and the blue star marks the Kangding earthquake, while the green star indicates historical earthquakes with magnitudes ≥ 6.5 in the past 300 years. The colored triangles denote the durations recorded by broadband seismic stations during the study period. The violet squares represent cities, and the black dots indicate the distribution of detected seismic activity. (b) The blue arrow represents the horizontal displacement derived from the Global Positioning System (GPS). Blue dots indicate GPS stations. The inset map indicates the regional tectonics.

On 5 September 2022, the moment magnitude (M_w) 6.7 Luding earthquake struck Luding County in Sichuan Province, China (Figure 1a). The seismic event triggered destructive landslides, resulting in 93 fatalities and significant economic losses [10]. The epicenter of the Luding earthquake (102.08°E , 29.59°N), as determined by the China Earthquake Networks Center, is located to the west of the Moxi section, and the depth range determined by different studies is 9–15 km [11]. The focal mechanism indicates that the earthquake is a left-lateral strike-slip rupture along a nearly vertical fault, consistent with the movement characteristics of the XSF. Complex fault structures are observed to the north and west of the mainshock, with aftershocks primarily distributed along the Moxi segment, filling the longstanding seismic gap in the region [12]. However, the event did not fully rupture the Moxi seismic gap.

The rupture process, as constrained by seismic data, shows that the Luding earthquake source duration was approximately 10 s and consisted of two distinct slippage sub-events. The rupture length along the strike was about 20 km, while the width along the dip gradually increased from north to south, reaching up to 20 km [13,14]. This is generally consistent with the slip distribution inverted from geodetic data [15,16]. The distribution of aftershocks along the XSF was discontinuous, with large normal-faulting aftershocks recorded in the Gongga Mountain region to the west of the mainshock, which may indicate a complex post-seismic process. Therefore, the analysis of the post-seismic process of the Luding earthquake is crucial for understanding the relationship between the kinematic characteristics of the fault zone and seismic activity, as well as for assessing the seismic hazard in the region.

In this study, we first obtained the static surface displacement using Interferometric Synthetic Aperture Radar (InSAR) measurements. Subsequently, deep learning techniques

were employed to generate a high-precision catalog of aftershocks. By integrating the coseismic slip distribution and the spatiotemporal distribution of aftershocks, we provide an interpretation of aftershock behavior, with the aim of discussing the fault geometry and kinematic properties, thereby enhancing the understanding of regional seismic hazard.

2. Materials and Methods

2.1. Coseismic Surface Deformation Processing

For this study, we used Sentinel-1/IW Interferometric Wide-Swath Synthetic Aperture Radar (SAR) data with a C-band operating frequency (wavelength of 5.6 cm). The imaging times for the main and auxiliary images of the descending track were 2 September and 14 September 2022. D-InSAR processing was performed using GMTSAR-V6.4 software on the pre- and post-earthquake image data [17]. First, the images were preprocessed, followed by image registration. Differential interferograms were then generated by removing the topographic phase and the flat earth phase using Digital Elevation Model (DEM) data of SRTM-1 s (30 m resolution, Shuttle Radar Topography Mission) and SAR orbit parameters. To suppress phase noise and enhance the signal-to-noise ratio, the interferograms were processed using multiple looking, with 8 looks in the azimuth direction and 2 looks in the range direction. Phase unwrapping was carried out using the minimum cost flow algorithm based on the Delaunay triangulation network [18]. To improve the unwrapping accuracy, a coherence threshold was applied prior to phase unwrapping, and areas with a coherence < 0.2 were masked. Additionally, areas with a coherence < 0.2 were also masked during geocoding.

2.2. Seismic Data Processing

We downloaded the continuous waveform records from broadband stations of the Sichuan Earthquake Administration, covering the period from 5 September 2022 to 1 October 2022, with a sampling rate of 100 Hz. A total of 46 stations along the Xianshuihe Fault (XSF) zone were selected for this study (Figure 1a). Of these, 39 stations recorded data for the entire period, while the remaining 7 stations recorded data for part of the period. Seismic detection and localization were performed on the raw data using the LOC-FLOW workflow [19]. This workflow is commonly employed for catalog detection in various regions. It consists of four main steps: phase picking, phase association, absolute location, and double-difference relative location.

First, a unified set of seismic phase pickers transfer-learned for China (USTC-Pickers) method is used for seismic phase picking [20]. This method employs the same U-Net architecture as PhaseNet [21] and is trained on the DiTing dataset in China, making it better suited for application within China. It can also be fine-tuned to adapt to different provinces. We input the original seismic waveform three-component data to obtain the probability distribution of the P/S phase at each moment. The P/S picking probability threshold selected is greater than 0.3. Second, the PyOcto method is applied to associate the picked seismic phases with individual events and perform a preliminary localization [22]. An event association is considered valid if it includes at least three P-phases and two S-phases, for a total of nine P+S-phases, and it requires data from at least two stations with both P- and S-phase observations (Figure 2). In the third step, the Hypoinverse method is used to localize all events [23], with the criteria set for travel time residuals less than 0.5 s and a station spacing less than 300 km. In the final step, double-difference tomography (tomoDD) is employed to achieve more precise earthquake locations [24]. Studies in the Southern Xiaojiang Fault zone have shown that tomoDD outperforms hypoDD [25,26]. The horizontal grid nodes of the study are set to a resolution of $0.1^\circ \times 0.1^\circ$, and the one-dimensional velocity model is derived from the reference 3D velocity structure SWChinaCVM-V2.0 [27].

Since high-resolution velocity structure results are available [28,29], the velocity model obtained from inversion is not utilized for further analysis in this study.

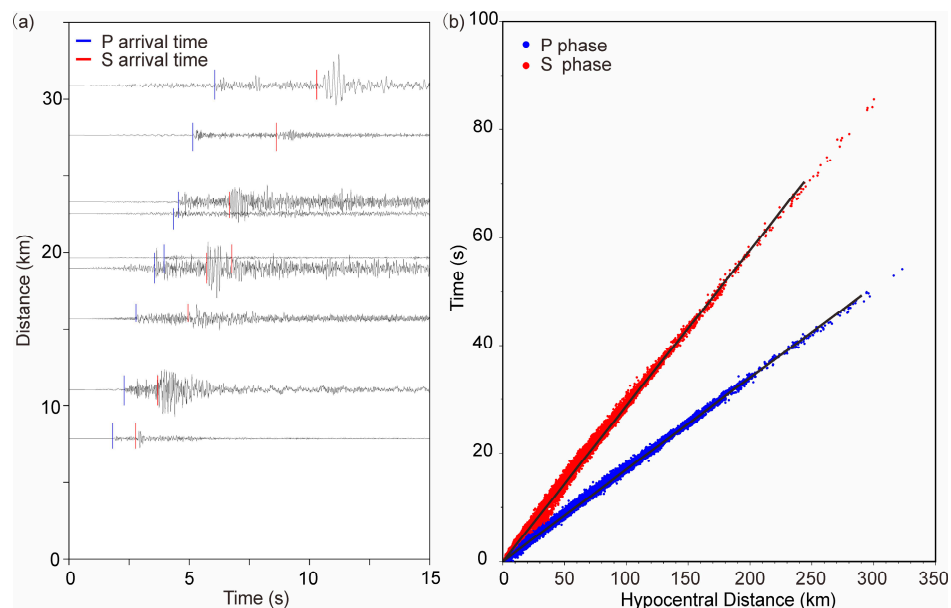


Figure 2. Phase picking and association. (a) An example of earthquake association using USTC-Pickers to determine the arrival times of the P-wave (blue line) and S-wave (red line). Only the vertical component of the waveform is displayed, and it is band-pass filtered in the frequency range of 1–10 Hz; (b) travel time–hypocentral distance curves for the associated events. The black line represents the fitted approximate velocities of the P-wave (6.0 km/s) and S-wave (3.5 km/s).

2.3. Catalog Comparison

Compared to the manual catalog, which contains 5045 events, we detected a total of 15,571 events, approximately three times as many. Of these, 4717 events, or nearly 93.5%, overlapped with the manual catalog, demonstrating the reliability of our detection process. The local magnitude (ML) of each earthquake event was calculated based on the relationship between the horizontal component of the S-wave amplitude and the magnitude [30]. The average magnitude difference between our catalog and the manual catalog was 0.2, with the corrected difference remaining within 0.5 (Figure 3a). A comparison with the manual catalog reveals that most of the detected events have magnitudes less than two (Figure 3b). Subsequently, we calculated the spatial distribution of release seismic moments [26].

2.4. Coseismic Slip Modeling

To simulate the Luding earthquake event, we employ the constrained least squares algorithm implemented in the Steepest Descent Method (SDM) program, which combines 74 GPS stations (Figure 1b) and descending track data to jointly invert the surface displacement associated with the coseismic slip [31], with a weighting ratio of 5:1 between the GPS data and the InSAR data. The initial strike of the fault is 162° , and the dip is 80° , as derived from the Global Centroid Moment Tensor (GCMT) source mechanism. The fault plane extends 80 km along the strike and 20 km along the dip. We discretize the fault into a series of sub-faults, each with dimensions of $2.5 \text{ km} \times 2.5 \text{ km}$. We also constrain the slip angle of the ruptured fault within a variable range, allowing the slip direction (slip angle) to vary [32]. In this inversion, the Green's function for the homogeneous elastic half-space model is calculated using the method described by Okada [33], assuming a Poisson's ratio of 0.25. We use the Stressinverse-V1.1.3 software to invert the stress directions based on the source mechanism solution [34,35]. The results indicate a compressive stress direction of

268.91° and a shear stress direction of 161.9°, which are consistent with the characteristics of left-lateral strike-slip.

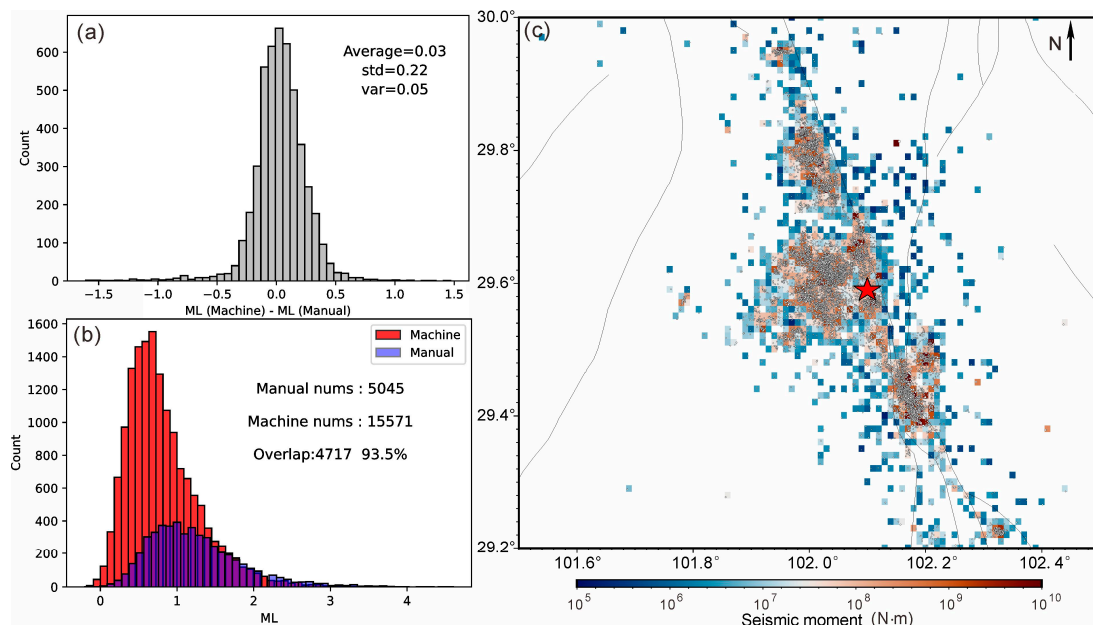


Figure 3. Comparison between the detected catalog and the manual catalog and the distribution of seismic release energy. (a) Distribution of magnitude differences between coexisting events after magnitude correction for both catalogs. (b) Characteristics of the magnitude–frequency distribution for the manual and detected catalogs. The red bars represent events identified by machine learning, while the blue bars correspond to events identified manually. (c) Distribution of seismic energy, with a grid size of $0.01^\circ \times 0.01^\circ$. The red star marks the location of the mainshock.

3. Results

3.1. Coseismic Deformation

From the processed coseismic deformation results (Figure 4), it can be observed that the deformation is primarily concentrated near the epicenter, with a maximum deformation of approximately 20 cm. A distinct deformation area is also observed in the southeast direction from the epicenter, extending about 15 cm. Due to the earthquake occurring in a mountainous region during the summer, when vegetation is dense and near a snow-capped mountain, InSAR coherence was significantly affected.

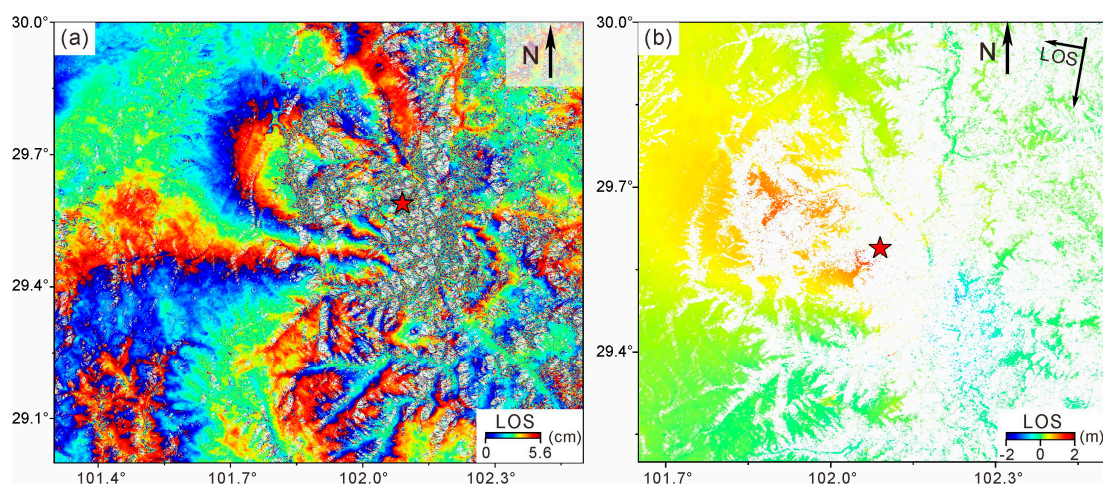


Figure 4. Sentinel-1 interferograms and line-of-sight (LOS) displacements from descending track. (a,b) The red stars indicate the location of the Luding earthquake.

3.2. Spatiotemporal Distribution of Aftershocks and Seismic Energy

The distribution of seismic moments generally correlates with seismic activity (Figure 3c). High seismic moment values are associated with areas of intense seismic activity and large earthquake magnitudes, which align closely with fault traces. Based on the spatial distribution of seismic activity and energy, four distinct low-energy zones (G1–G4) have been identified from north to south (Figure 5).

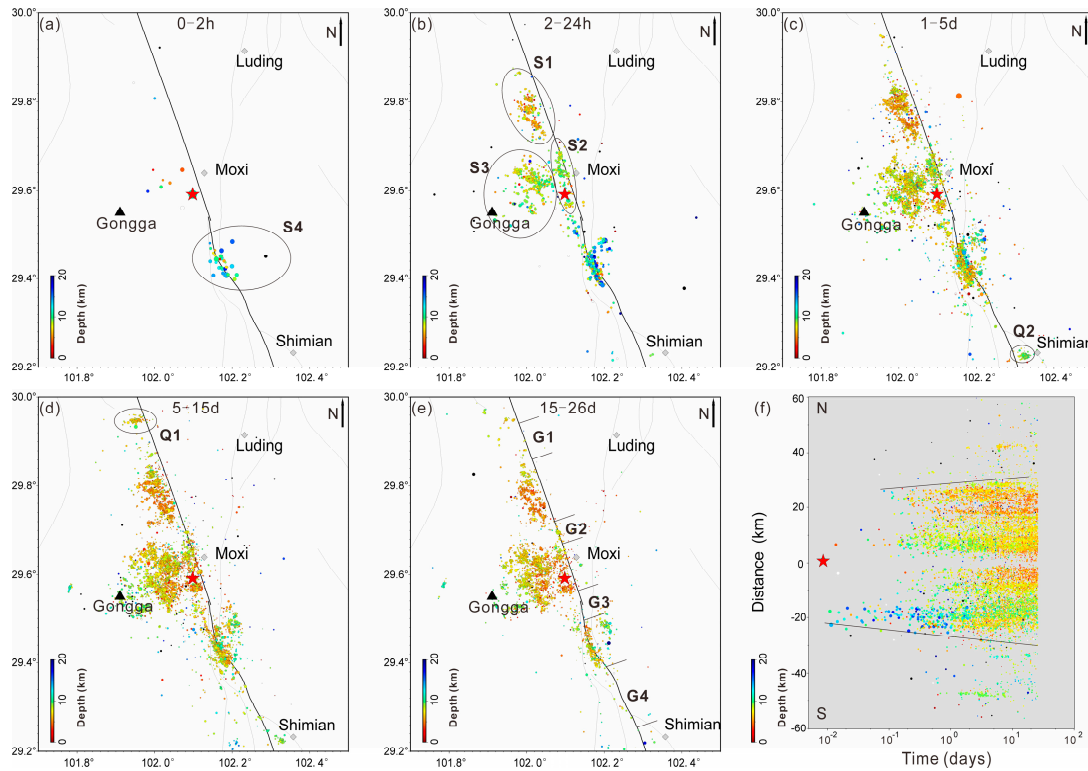


Figure 5. Spatial distribution of aftershocks at different times. (a–e) Aftershock activity is shown by colored dots, with the color representing depth. The red star is the location of the mainshock. The black circles indicate divided aftershock groups (S1–S4), and the black lines divide aftershock gaps (G1–G4). (f) Spatial–temporal aftershock evolution. The solid black line shows the direction of expansion of seismic activity over time.

The aftershock distribution is primarily concentrated to the west, northwest, and southeast of the mainshock, covering a total length of approximately 80 km. The earthquake depth in the west and northwest (<15 km) is shallower than in the southeast (<20 km). Overall, the aftershock region can be divided into four main segments (S1–S4, Figure 5). S1 is located to the northwest of the mainshock, aligned with the regional trend but predominantly situated on the western side of the surface trace of the Xianshuihe Fault zone (XSF). S2 is distributed near the mainshock and along the XSF. S3 is found in the Gongga Mountains to the west of the mainshock, where aftershocks are more widely scattered, lacking a clear spatial trend, though seismic activity becomes progressively more frequent from west to east. S4 is located southeast of the mainshock, along the XSF, and represents the intersection of several fault zones: the Longmenshan, Xianshuihe, Anninghe, and Xiaojinhe Faults. There were small aftershocks to the east of S4. In particular, two small clusters of aftershocks were observed: one to the north of S1 and the other to the south of S4 (denoted as Q1 and Q2, Figure 5c,d). In terms of timing, aftershocks near S4 were quickly triggered following the mainshock, with aftershocks in the S1–S3 region activating two hours later, gradually spreading throughout the area. Seismic activity then began to occur in the northernmost Q1 and the southernmost Q2 two days later. After fifteen days,

the activity weakened, and Q2 had essentially returned to calm. Over time, seismic activity in the S3 region, particularly within Gongga Mountain, became progressively more active from east to west.

3.3. Fault Structure

To study the geometry of the complex fault system revealed by the sequence of aftershocks triggered by the Luding earthquake, we used the AVF-V0.1 program to fit the fault morphology [36]. The Local Outlier Factor (LOF) analysis algorithm, based on local density, was applied to filter out outlier points in the aftershock cluster, thereby improving the fitting of the fault plane [37]. In this context, a data point is considered anomalous if its density is significantly lower than that of its neighbors.

We first analyzed the two aftershock clusters, Q1 and Q2, which are the farthest from the mainshock. For Q1, located to the west of the XSF, the cross-section AA' (Figure 6k) reveals a nearly vertical fault. The aftershock depth ranges from 7 to 10 km, with a dip angle of 81.6° and a strike of 75.32° . For Q2, it is located between the Xianshuihe Fault and the Daliangshan Fault, with aftershocks occurring at depths of 7–11 km. The cross-sections II' and JJ' (Figure 6i,j) characterize the geometric shape of the fault. The fitting results indicate a dip angle of 79.68° and a strike of 135.19° . Both are concealed faults. The concealed fault strike in Q1 is nearly vertical to the strike of the Xianshuihe Fault, reflecting lateral extrusion from the blockage of the Sichuan Basin. The intersecting fault structures may contribute to an unstable regional stress state, making the area more prone to seismic activity. The concealed faults in Q2 are approximately parallel to the strike of the Xianshuihe Fault, suggesting the possible existence of a rupture zone between the Xianshuihe Fault and the Daliangshan Fault.

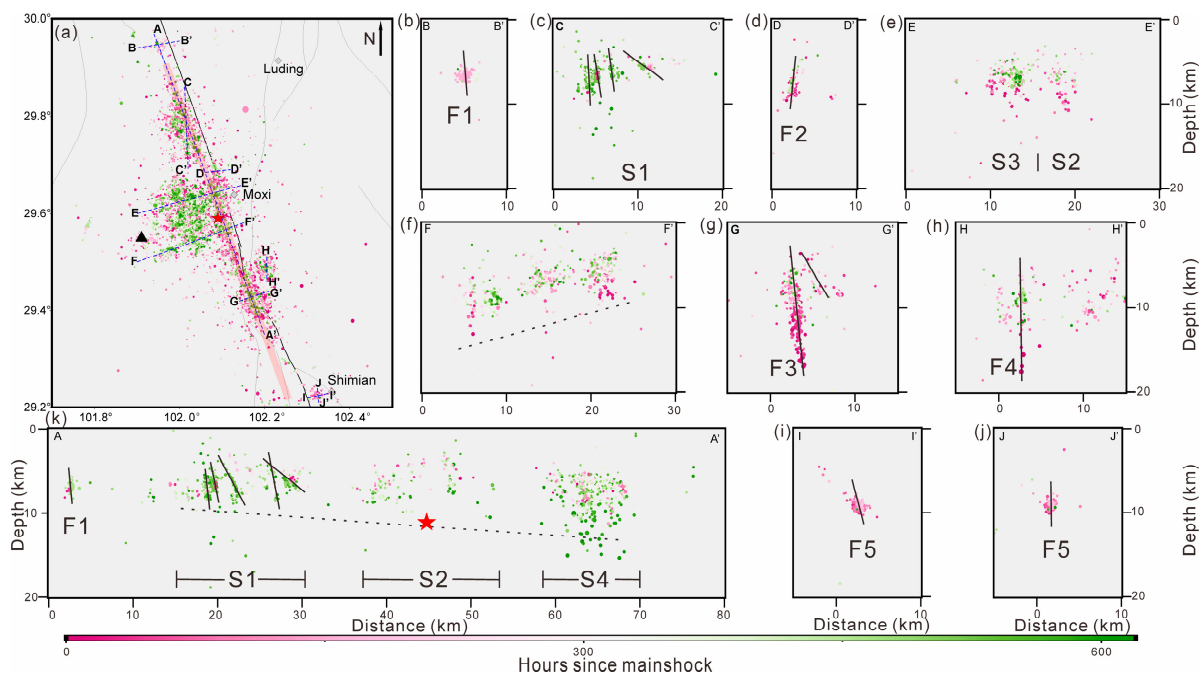


Figure 6. Regional fault profile. (a) The dashed blue line indicates the cross-section profiles, the red star indicates the location of the mainshock, and the black triangle indicates the Gongga Mountain. The red surface indicates the fault plane used to invert the coseismic slip. (b–k) The solid black line indicates the fault fit, and the parameters are given in the text. The dashed black line indicates the trend of changes in the depth of seismic activity. The time in hours until aftershocks occur is indicated by the color.

After that, S1–S4, which are closer to the mainshock, were fitted. Overall, the aftershocks reveal a complex fault system along the cross-section AA'. To the north of the mainshock, the aftershock activity occurs at relatively shallow depths, ranging from 5 to 11 km, while to the south, the depth increases, reaching about 17 km at S3 in particular. The aftershock distribution at S1 is complex and difficult to model. Located on the western side of the XSF, S1 shows multiple small faults with inconsistent strikes. Combining cross-sections AA' and CC' (Figure 6c) reveals a series of near-vertical and individual near-horizontal concealed faults. The fault strikes indicated by the aftershock distribution are not uniform, and the angle of intersection with the main fault gradually increases from south to north. S2 gradually moves away from the main fault from north to south. Cross-section DD' (Figure 6d) reveals the geometric structure of this section of the XSF. The fitted dip angle is 87.48° , and the strike is 166.56° , which is consistent with the main fault's dip angle of 80° W. The aftershock activity to the north of the mainshock does not allow for a clear constraint on the fault morphology based on the cross-section EE' (Figure 6e). The depths of the aftershocks are relatively uniform, with most occurring above 10 km. To the south of the mainshock, aftershock activity, as shown in the cross-section FF' (Figure 6f), gradually becomes shallower from west to east, consistent with the southwestward dip of the main fault. The aftershock activity in S3 is highly irregular, making it difficult to delineate the fault morphology and activity trends. In contrast, aftershock activity in S4 is well-distributed along the main fault, with a small cluster of aftershocks located to the east. The cross-section GG' (Figure 6g) reveals two faults: on the west side, the main fault of the XSF, and on the east side, likely the Daduhe Fault. The main fault has a fitted dip angle of 87.58° and a strike of 337.25° . Cross-section HH' (Figure 6h) shows some aftershock activity to the east, where a northeast-dipping fault with a fitted dip angle of 89.15° and a strike of 275.59° .

3.4. Coseismic Slip Distribution and Static Stress Changes

The main rupture of the Luding earthquake is located in the Moxi section of the Xianshuihe Fault, with the coseismic slip concentrated at depths of 0–10 km, extending to the surface (Figure 7a). The depth of the slippage increases gradually from north to south, reaching a maximum of 15 km. Along the fault strike, the coseismic slip exhibits a characteristic pattern, with a lower slip in the north and higher slip in the south, and a maximum slip of ~2 m. Inversion results yield a total M_w of 6.69 for the earthquake, which is consistent with the moment magnitude reported by the GCMT. Earthquake ruptures inevitably induce stress changes in surrounding areas, which are often analyzed to study the spatiotemporal evolution of subsequent seismic events [38–40]. In this study, we calculate the shear stress changes on the fault plane caused by the Luding earthquake's fault slip (Figure 7b). To explain the primary left-lateral strike-slip, we adopt a fixed static friction coefficient of 0.4, which is a typical value of inland strike-slip faults, and assume shear modulus and Poisson's ratio values of 33 GPa and 0.25, respectively [41]. The results of the shear stress change show that the stress distribution is basically the opposite of the slip distribution. Areas with large slips are mainly characterized by stress suppression, while the shallow part of the north side of the slip and the south side are characterized by stress loading.

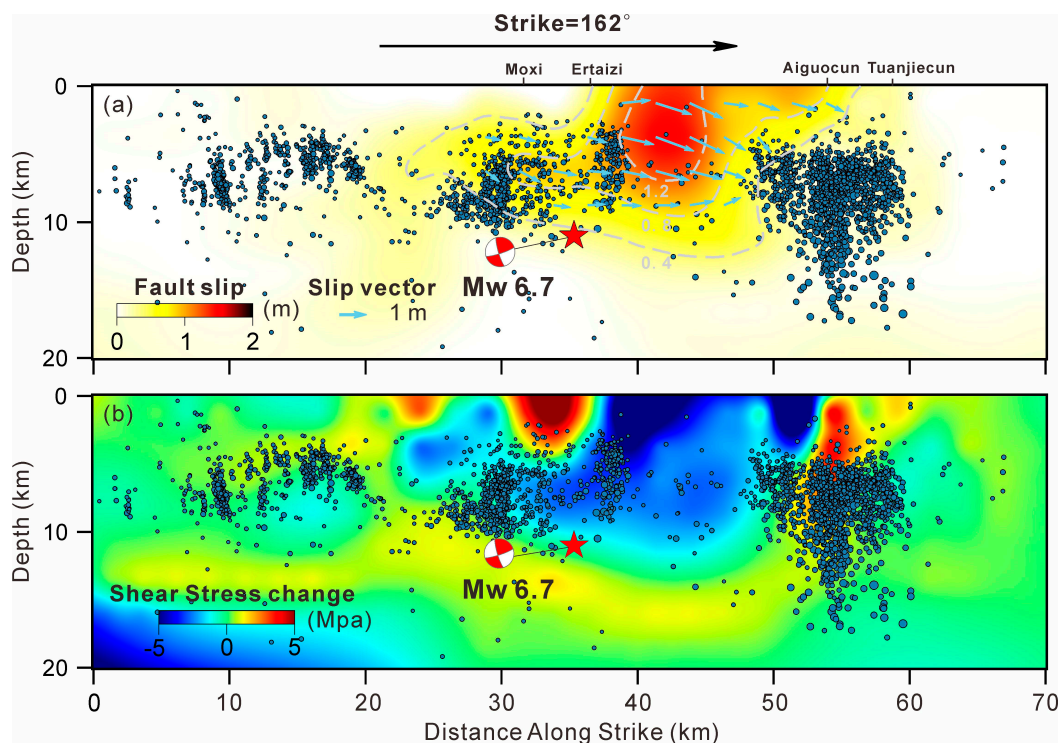


Figure 7. Coseismic slip model and shear stress changes for the Luding earthquake. (a) The blue arrows indicate the direction of the slip, with the length representing the amount of slippage. The gray dashed lines represent contours of equal slippage. (b) The red star indicates the epicenter, and the red beach ball indicates the source mechanism solution.

4. Discussion

4.1. Temporal and Spatial Variation of Coseismic Slip and Aftershock

Normally, the areas of coseismic slip and aftershock activity are complementary [13–16]. Coseismic rupture releases stress through slippage, leading to sparse aftershock activity. However, in the regions where slippage transitions to locking, stress is released in the form of aftershocks, which show distinct spatial distribution patterns. In this study, we plot the aftershock activity over different time segments onto the coseismic slip model for further analysis (Figure 8).

The slip distribution models derived from seismology and geodesy are generally consistent for the Luding earthquake [13–16]. Most aftershocks are distributed along the edges of the coseismic slip, while a few are located in areas of large slippage. These patterns have been observed in other studies and reflect a strong stress release within the rupture zone, with a concentration of activity at the rupture boundaries [42,43]. Two hours after the mainshock, aftershock activity began to increase first in the S4 region on the southern side, with a higher aftershock rate compared to the epicenter. Additionally, the aftershocks occurred at significantly greater depths, suggesting a static triggering effect [44–47]. Two hours after the mainshock, aftershocks around the epicenter became active. Based on the distribution of shear stress along the fault, this may indicate that the stress accumulated along the boundary during coseismic slip had begun to trigger ruptures in the surrounding area. After 24 h, aftershock activity in region S2 continued to spread, with sparsely distributed aftershocks occurring above the epicenter. Aftershock activity in the southern region, S4, also began to shift to shallower depths and moved closer to the slippage of A2. It is likely that the aftershocks in this region were triggered by Coulomb stress changes induced by the earthquake, which released the accumulated stress before re-locking occurred. A post-earthquake afterslip may have further promoted the accumulation

of stress in the vicinity, triggering additional aftershocks. The spatiotemporal distribution of aftershock activity reveals that aftershocks in the S4 segment exhibited a logarithmic migration to the south, suggesting a mechanism driven by an afterslip [14,48,49].

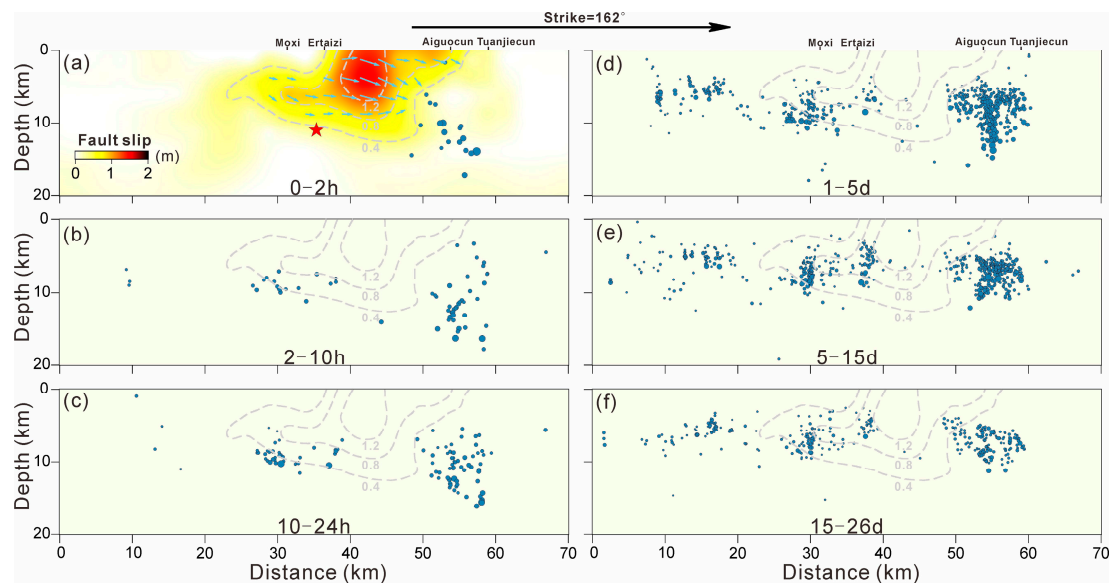


Figure 8. The relationship between coseismic slip and the distribution of aftershocks at different times. (a–f) The steel-blue dots indicate aftershocks; The gray dashed lines represent contours of equal slippage; Red star indicates the location of the Luding earthquake.

Combining the results of the aftershock activity and coseismic slip, we speculate that the S4 aftershocks are immediately activated by the triggering of coseismic Coulomb stress during the coseismic slip. Once the slippage ends, aftershocks in S2 become active due to stress driving, while S4 aftershocks are then driven by an afterslip. This results in different rates of aftershock activity and depth distributions between S2 and S4. The aftershock activity in the region above the mainshock is more frequent than in the southern slippage area, which may suggest a higher degree of fault coupling in the northern section compared to the southern section.

4.2. Complex Fault as Revealed by Aftershock

The distribution of aftershock activity reveals distinct gaps (G1–G4) around S1, S2, and S4, which may reflect the heterogeneity of the fault. Numerous studies have shown that the mainshock typically occurs in the transition zone between high and low resistivity [50–52]. By combining a 3D resistivity model [53], the mainshock was found to occur in an area characterized by a clear transition between high and low resistivity (Figure 9b). G2 is located north of the mainshock and is characterized by high resistivity, with a decrease in resistivity on the western side. The low-frequency aftershock activity in this area suggests that the cumulative stress may not be sufficient to trigger a rupture, and the stress continues to propagate northward. S2, located in a boundary zone between high and low resistivity (Figure 9d), is associated with a complex fault system that indicates the presence of previous ruptures. As a result, the cumulative stress in this area is more likely to lead to future ruptures. As for G3, located in the southern part of the mainshock, it is characterized by a distinct low-resistivity body (Figure 9b). Under normal conditions, low-resistivity rock masses generally exhibit weak mechanical properties, which are not conducive to stress accumulation. Additionally, G3 lies within the rupture zone of the coseismic slip, where most of the stress has already been released, making further ruptures unlikely. However,

low-resistivity is more prone to deformation and may continue to undergo afterslips, potentially triggering aftershock activity in the S4.

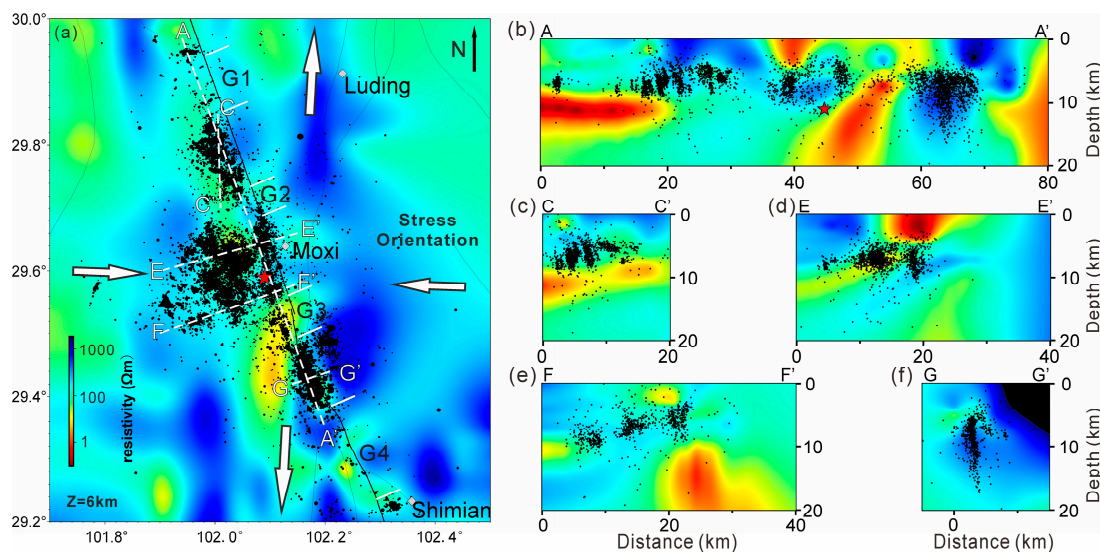


Figure 9. A 3D resistivity structure depth slice. (a) Black dots indicate aftershocks, and red stars indicate the mainshock. The white arrow indicates the stress direction derived from the inversion of the source mechanism. (b–f) Cross-sections of resistivity structure.

Both G1 and G4 exhibit characteristics of low resistivity in the deep and high resistivity in the shallow. This structural configuration is prone to stress accumulation and rupture. The weak aftershock activity suggests that the stress released by the Luding earthquake was insufficient to induce rupture in these areas. However, the resistivity of the shallow G1 is lower than that of G4, which implies that the mechanisms for aftershock termination may differ between the northern and southern sides. It is generally believed that fault slip is the primary factor inhibiting rupture. The interseismic fault coupling model indicates that the faults in Ludin are almost entirely locked at depths shallower than 20 km [54]. However, the higher aftershock rate and broader depth distribution observed in S4 may suggest that the southern part of the fault is not fully locked and could act as a frictional barrier. Additionally, the main fault trend derived from S4 differs from that fitted by S2, indicating the geometric complexity of the regional fault structure. This complexity may also contribute to the termination of aftershocks. The G1 structure is challenging to interpret, particularly the series of concealed faults in S1. Based on the combined results of the resistivity and velocity profiles [28], the eastern side of the aftershock zone exhibits high resistance and high velocity, which may indicate the presence of intermediate to intermediate–basic intrusive rocks [55]. This could also provide an explanation for the formation of the regional east–west strike faults. Such a fault system may act as a geometric barrier, similar to fault stepovers [56,57] and branching faults [58].

The fault structures and properties within each aftershock gap vary, indicating a strong heterogeneity of faults in the study area. The coupling state may also exhibit significant changes, which require further explanation in conjunction with the characteristics of long-term seismic activity and source mechanisms.

4.3. Seismic Hazard Assessment

Due to the uncertainty of the InSAR deformation, the state of creep in the Xianshuihe Fault zone (XSF) in the study area cannot be reliably assessed. According to the Coulomb failure law [59], when an earthquake occurs, it alters the stress state of surrounding active faults, thereby either triggering or suppressing seismic hazards on nearby faults. The

results of our calculations, along with the Δ CFS distributions obtained using different methods [14,15], indicate that stress accumulation exists at G2 and G4, and studies of the effects of historical earthquakes also reveal the possibility of large stress accumulations in both regions [60,61]. G2, located on the north side, is located in a region characterized by transitions in both high and low resistivity and velocity. The b-value prior to the earthquake was >1 [62], suggesting that the region did not accumulate significant stress before the earthquake. However, it may accumulate stress after the earthquake and has the potential to incubate a major earthquake.

G4 on the southern side exhibits significant stress accumulation and is located in a transition zone between high and low resistivity and velocity, with a complex fault structure. The b-value prior to the earthquake was <0.8 , indicating that the area had already experienced a high level of stress. Some of the aftershocks can only release part of the accumulated stress. The Xianshuihe Fault intersects the Anninghe Fault in this region. The last major event in the area was an M 7.5 earthquake in 1480, and no major events have occurred in the past 540 years. Recent studies of the Anninghe Fault have shown that the northern section exhibits both seismic and non-seismic slip modes, with deep creep driving active microseismicity. In contrast, the southern section remains locked, suggesting that an M7+ earthquake could potentially occur. Therefore, the Luding earthquake may have influenced the unruptured G2 and G4 sections, increasing the likelihood of future seismic hazards.

5. Conclusions

In this study, we integrate InSAR and GPS data to jointly constrain the coseismic slip distribution and apply machine learning to process raw seismic wave data, constructing a high-quality aftershock catalog. The complex geometry and kinematics of the Luding earthquake fault system were analyzed by examining the relationship between aftershock spatiotemporal distribution and coseismic slip, providing insights into the rupture characteristics. The rupture was dominated by left-lateral strike-slip motion, with fault slip concentrated at depths shallower than 10 km and near the surface. Aftershock activity deepens progressively from north to south within the coseismic slip region. In the no-slip zone to the north, a complex hidden fracture system exists. The fault geometry of the Xianshuihe Fault is inconsistent between the mainshock and the southern part near the Anninghe Fault. Aftershock clusters on the southern part show logarithmic migration, suggesting a mechanism driven by afterslip, indicates a low fault coupling, with stress potentially accumulating to the south, leading to an increased seismic hazard. Resistivity and velocity structure analysis suggest that aftershock termination may be influenced by both the fault's geometry and its intrinsic properties. A comprehensive analysis indicates that the seismic gaps to the north of the mainshock and to the south, near the Anninghe Fault, may pose higher seismic hazard.

Author Contributions: Conceptualization, Q.H. and G.Z.; methodology, Q.H.; validation, G.Z., X.S. and H.L. (Hongyi Li); formal analysis, Q.H.; investigation, Q.H. and H.L. (Hongwei Liang); data curation, Q.H. and H.L. (Hongwei Liang); writing—original draft preparation, Q.H.; writing—review and editing, Q.H.; visualization, Q.H.; supervision, G.Z.; project administration, G.Z.; funding acquisition, G.Z. All authors have read and agreed to the published version of the manuscript.

Funding: This research was co-funded by the Basic Scientific Funding of the Institute of Geology, China Earthquake Administration (Grant No. IGCEA2005) and the National Natural Science Foundation of China (Grant No. U2139202).

Data Availability Statement: The raw data supporting the conclusions of this article will be made available by the authors on request.

Acknowledgments: We thank the editor and the five anonymous reviewers for their constructive suggestions that significantly improved the quality of the manuscript. We thank the Sichuan Earthquake Administration for providing the raw seismic wave data.

Conflicts of Interest: The authors declare no conflicts of interest.

References

1. Allen, C.R.; Zhuoli, L.; Hong, Q.; Xueze, W.; Huawei, Z.; Weishi, H. Field Study of a Highly Active Fault Zone: The Xianshuihe Fault of Southwestern China. *Geol. Soc. Am. Bull.* **1991**, *103*, 1178–1199. [[CrossRef](#)]
2. Wen, X.; Fan, J.; Yi, G.; Deng, Y.; Long, F. A Seismic Gap on the Anninghe Fault in Western Sichuan, China. *Sci. China Ser. D-Earth Sci.* **2008**, *51*, 1375–1387. [[CrossRef](#)]
3. Bai, M.; Chevalier, M.L.; Pan, J.; Replumaz, A.; Leloup, P.H.; Métois, M.; Li, H. Southeastward Increase of the Late Quaternary Slip-Rate of the Xianshuihe Fault, Eastern Tibet. Geodynamic and Seismic Hazard Implications. *Earth Planet. Sci. Lett.* **2018**, *485*, 19–31. [[CrossRef](#)]
4. Guo, R.; Zheng, Y.; Tian, W.; Xu, J.; Zhang, W. Locking Status and Earthquake Potential Hazard along the Middle-South Xianshuihe Fault. *Remote Sens.* **2018**, *10*, 2048. [[CrossRef](#)]
5. Qiao, X.; Zhou, Y. Geodetic Imaging of Shallow Creep along the Xianshuihe Fault and Its Frictional Properties. *Earth Planet. Sci. Lett.* **2021**, *567*, 117001. [[CrossRef](#)]
6. Li, Y.; Bürgmann, R. Partial Coupling and Earthquake Potential Along the Xianshuihe Fault, China. *JGR Solid Earth* **2021**, *126*, e2020JB021406. [[CrossRef](#)]
7. Wen, X.; Ma, S.; Xu, X.; He, Y. Historical Pattern and Behavior of Earthquake Ruptures along the Eastern Boundary of the Sichuan-Yunnan Faulted-Block, Southwestern China. *Phys. Earth Planet. Inter.* **2008**, *168*, 16–36. [[CrossRef](#)]
8. Xu, X.; Wu, X.; Yu, G.; Tan, X.; Li, K. Seismo-geological signatures for identifying $M \geq 7.0$ earthquake risk areas and their preliminary application in mainland China. *Seismol. Geol.* **2017**, *39*, 219–275. [[CrossRef](#)]
9. Shao, Z.; Wu, Y.; Ji, L.; Diao, F.; Shi, F.; Li, Y.; Long, F.; Zhang, H.; Wang, W.; Wei, W.; et al. Assessment of Strong Earthquake Risk in the Chinese Mainland from 2021 to 2030. *Earthq. Res. Adv.* **2023**, *3*, 100177. [[CrossRef](#)]
10. Qu, Z.; Zhu, B.; Cao, Y.; Fu, H. Rapid Report of Seismic Damage to Buildings in the 2022 M 6.8 Luding Earthquake, China. *Earthq. Res. Adv.* **2023**, *3*, 100180. [[CrossRef](#)]
11. Yao, Q.; Yu, C.; Zeng, X. Shallow Focal Depths of the 2022 Ms 6.8 Luding Earthquake and Its $M \geq 3$ Aftershocks. *Seismol. Res. Lett.* **2024**, 1–17. [[CrossRef](#)]
12. Xu, X.; Wang, Q.; Ren, J.; Li, K.; Yao, Q.; Xu, C.; Li, Y.; An, Y.; Cheng, J. Three-Dimensional Fault Model and Features of Chained Hazards of the Luding Ms 6.8 Earthquake, Sichuan Province, China. *Earthq. Res. Adv.* **2024**, *4*, 100326. [[CrossRef](#)]
13. Zhao, X.; Xiao, Z.; Wang, W.; Li, J.; Zhao, M.; Chen, S.; Tang, L. Fine Seismogenic Fault Structures and Complex Rupture Characteristics of the 2022 M 6.8 Luding, Sichuan Earthquake Sequence Revealed by Deep Learning and Waveform Modeling. *Geophys. Res. Lett.* **2023**, *50*, e2023GL102976. [[CrossRef](#)]
14. Zhang, L.; Zhou, Y.; Zhang, X.; Zhu, A.; Li, B.; Wang, S.; Liang, S.; Jiang, C.; Wu, J.; Li, Y.; et al. 2022 Mw 6.6 Luding, China, Earthquake: A Strong Continental Event Illuminating the Moxi Seismic Gap. *Seismol. Res. Lett.* **2023**, *94*, 2129–2142. [[CrossRef](#)]
15. Li, Y.; Zhao, D.; Shan, X.; Gao, Z.; Huang, X.; Gong, W. Coseismic Slip Model of the 2022 Mw 6.7 Luding (Tibet) Earthquake: Pre- and Post-Earthquake Interactions With Surrounding Major Faults. *Geophys. Res. Lett.* **2022**, *49*, e2022GL102043. [[CrossRef](#)]
16. Guo, R.; Li, L.; Zhang, W.; Zhang, Y.; Tang, X.; Dai, K.; Li, Y.; Zhang, L.; Wang, J. Kinematic Slip Evolution During the 2022 Ms 6.8 Luding, China, Earthquake: Compatible With the Preseismic Locked Patch. *Geophys. Res. Lett.* **2023**, *50*, e2023GL103164. [[CrossRef](#)]
17. Sandwell, D.; Mellors, R.; Tong, X.; Wei, M.; Wessel, P. Open Radar Interferometry Software for Mapping Surface Deformation. *EoS Trans.* **2011**, *92*, 234. [[CrossRef](#)]
18. Werner, C.; Wegmüller, U.; Strozzi, T.; Wiesmann, A. Processing strategies for phase unwrapping for INSAR applications. In Proceedings of the European Conference on Synthetic Aperture Radar EUSAR 2002, Cologne, Germany, 4–6 June 2002; Gamma Remote Sensing AG: Muri bei Bern, Switzerland, 2002; Volume 1, pp. 353–356.
19. Zhang, M.; Liu, M.; Feng, T.; Wang, R.; Zhu, W. LOC-FLOW: An End-to-End Machine Learning-Based High-Precision Earthquake Location Workflow. *Seismol. Res. Lett.* **2022**, *93*, 2426–2438. [[CrossRef](#)]
20. Zhu, J.; Li, Z.; Fang, L. USTC-Pickers: A Unified Set of Seismic Phase Pickers Transfer Learned for China. *Earthq. Sci.* **2023**, *36*, 95–112. [[CrossRef](#)]
21. Zhu, W.; Beroza, G.C. PhaseNet: A Deep-Neural-Network-Based Seismic Arrival Time Picking Method. *Geophys. J. Int.* **2018**, *216*, 261–273. [[CrossRef](#)]
22. Münchmeyer, J. PyOcto: A High-Throughput Seismic Phase Associator. *Seismica* **2024**, *3*, 1. [[CrossRef](#)]

23. Klein, F.W. *User's Guide to HYPOINVERSE-2000, a Fortran Program to Solve for Earthquake Locations and Magnitudes*; Open-File Rept. 02-171; U.S. Geological Survey: Menlo Park, CA, USA, 2002; Volume 1. [\[CrossRef\]](#)
24. Zhang, H.; Thurber, C. Development and Applications of Double-Difference Seismic Tomography. *Pure Appl. Geophys.* **2006**, *163*, 373–403. [\[CrossRef\]](#)
25. Waldhauser, F. A Double-Difference Earthquake Location Algorithm: Method and Application to the Northern Hayward Fault, California. *Bull. Seismol. Soc. Am.* **2000**, *90*, 1353–1368. [\[CrossRef\]](#)
26. Feng, T.; Zhang, M.; Xu, L.; Wu, J.; Fang, L. Machine Learning-Based Earthquake Catalog and Tomography Characterize the Middle-Northern Section of the Xiaojiang Fault Zone. *Seismol. Res. Lett.* **2022**, *93*, 2484–2497. [\[CrossRef\]](#)
27. Liu, Y.; Yu, Z.; Zhang, Z.; Yao, H.; Wang, W.; Zhang, H.; Fang, H.; Fang, L. The High-Resolution Community Velocity Model V2.0 of Southwest China, Constructed by Joint Body and Surface Wave Tomography of Data Recorded at Temporary Dense Arrays. *Sci. China Earth Sci.* **2023**, *66*, 2368–2385. [\[CrossRef\]](#)
28. Cai, G.; Wang, W.; Wu, J.; Su, J.; Lai, G.; Wu, P.; Chen, L.; Su, J. Three-Dimensional Body Wave Velocity Structure and Seismogenic Structure for the 2022 MS 6.8 Luding Earthquake Sequence in Sichuan, China. *Front. Earth Sci.* **2023**, *11*, 1099744. [\[CrossRef\]](#)
29. Cai, M.; Chen, J.; Yin, X. Three-dimensional Velocity Structure and Relocation of Earthquakes in Luding area, Sichuan Province. *China Earthq. Eng. J.* **2023**, *45*, 552–564. [\[CrossRef\]](#)
30. Hutton, L.K.; Boore, D.M. The *ML* Scale in Southern California. *Bull. Seismol. Soc. Am.* **1987**, *77*, 2074–2094. [\[CrossRef\]](#)
31. Wang, R.; Parolai, S.; Ge, M.; Jin, M.; Walter, T.R.; Zschau, J. The 2011 Mw 9.0 Tohoku Earthquake: Comparison of GPS and Strong-Motion Data. *Bull. Seismol. Soc. Am.* **2013**, *103*, 1336–1347. [\[CrossRef\]](#)
32. Li, C.; Shan, X.; Zhang, G.; Zhao, C.; Gong, W.; Zhang, Y. Slip Kinematics of the 2021 Yangbi Earthquake: Fore-Main-Aftershock Sequence Rupture along an Unknown Secondary Fault of the Weixi–Qiaohou Fault. *Seismol. Res. Lett.* **2022**, *93*, 1400–1412. [\[CrossRef\]](#)
33. Okada, Y. Surface deformation due to shear and tensile faults in a half-space. *Bull. Seismol. Soc. Am.* **1985**, *75*, 1135–1154. [\[CrossRef\]](#)
34. Vavryčuk, V. Iterative Joint Inversion for Stress and Fault Orientations from Focal Mechanisms. *Geophys. J. Int.* **2014**, *199*, 69–77. [\[CrossRef\]](#)
35. Vavryčuk, V. Principal Earthquakes: Theory and Observations from the 2008 West Bohemia Swarm. *Earth Planet. Sci. Lett.* **2011**, *305*, 290–296. [\[CrossRef\]](#)
36. Wang, C.; Ke, J.; Jiang, J.; Lu, M.; Xiu, W.; Liu, P.; Li, Q. Visual Analytics of the Aftershock Point Cloud Data in Complex Fault Systems. *Solid Earth Discuss.* **2019**, *10*, 1397–1407. [\[CrossRef\]](#)
37. Breunig, M.M.; Kriegel, H.-P.; Ng, R.T.; Sander, J. LOF: Identifying Density-Based Local Outliers. *Int. Conf. Manag. Data* **2000**, *29*, 93–104.
38. Lin, J.; Stein, R.S. Stress Triggering in Thrust and Subduction Earthquakes and Stress Interaction between the Southern San Andreas and Nearby Thrust and Strike-slip Faults. *J. Geophys. Res.* **2004**, *109*, 2003JB002607. [\[CrossRef\]](#)
39. Toda, S.; Stein, R.S.; Richards-Dinger, K.; Bozkurt, S.B. Forecasting the Evolution of Seismicity in Southern California: Animations Built on Earthquake Stress Transfer. *J. Geophys. Res.* **2005**, *110*, 2004JB003415. [\[CrossRef\]](#)
40. Herman, M.W.; Herrmann, R.B.; Benz, H.M.; Furlong, K.P. Using Regional Moment Tensors to Constrain the Kinematics and Stress Evolution of the 2010–2013 Canterbury Earthquake Sequence, South Island, New Zealand. *Tectonophysics* **2014**, *633*, 1–15. [\[CrossRef\]](#)
41. Freed, A.M.; Ali, S.T.; Bürgmann, R. Evolution of Stress in Southern California for the Past 200 Years from Coseismic, Postseismic and Interseismic Stress Changes. *Geophys. J. Int.* **2007**, *169*, 1164–1179. [\[CrossRef\]](#)
42. Gallovič, F.; Zahradník, J.; Plicka, V.; Sokos, E.; Evangelidis, C.; Fountoulakis, I.; Turhan, F. Complex Rupture Dynamics on an Immature Fault during the 2020 Mw 6.8 Elazığ Earthquake, Turkey. *Commun. Earth Environ.* **2020**, *1*, 40. [\[CrossRef\]](#)
43. Toda, S.; Stein, R.S. Central Shutdown and Surrounding Activation of Aftershocks from Megathrust Earthquake Stress Transfer. *Nat. Geosci.* **2022**, *15*, 494–500. [\[CrossRef\]](#)
44. King, G.C.P.; Stein, R.S.; Lin, J. Static Stress Changes and the Triggering of Earthquakes. *Bull. Seismol. Soc. Am.* **1994**, *84*, 935–953. [\[CrossRef\]](#)
45. Toda, S.; Stein, R.S.; Reasenberg, P.A.; Dieterich, J.H.; Yoshida, A. Stress Transferred by the 1995 $M_w = 6.9$ Kobe, Japan, Shock: Effect on Aftershocks and Future Earthquake Probabilities. *J. Geophys. Res.* **1998**, *103*, 24543–24565. [\[CrossRef\]](#)
46. Stein, R.S. The Role of Stress Transfer in Earthquake Occurrence. *Nature* **1999**, *402*, 605–609. [\[CrossRef\]](#)
47. Seeber, L.; Armbruster, J.G. Earthquakes as Beacons of Stress Change. *Nature* **2000**, *407*, 69–72. [\[CrossRef\]](#)
48. Peng, Z.; Zhao, P. Migration of Early Aftershocks Following the 2004 Parkfield Earthquake. *Nat. Geosci.* **2009**, *2*, 877–881. [\[CrossRef\]](#)
49. Jiang, J.; Bock, Y.; Klein, E. Coevolving Early Afterslip and Aftershock Signatures of a San Andreas Fault Rupture. *Sci. Adv.* **2021**, *7*, eabc1606. [\[CrossRef\]](#)
50. Chen, C.-S.; Chen, C.-C. Magnetotelluric Soundings of the Source Area of the 1999 Chi-Chi Earthquake in Taiwan: Evidence of Fluids at the Hypocenter. *Terr. Atmos. Ocean. Sci.* **2000**, *11*, 679. [\[CrossRef\]](#)

51. Zhao, G.; Unsworth, M.J.; Zhan, Y.; Wang, L.; Chen, X.; Jones, A.G.; Tang, J.; Xiao, Q.; Wang, J.; Cai, J.; et al. Crustal Structure and Rheology of the Longmenshan and Wenchuan Mw 7.9 Earthquake Epicentral Area from Magnetotelluric Data. *Geology* **2012**, *40*, 1139–1142. [[CrossRef](#)]
52. Cheng, Y.; Tang, J.; Cai, J.; Chen, X.; Dong, Z.; Wang, L. Deep electrical structure beneath the Sichuan-Yunnan area in the eastern margin of the Tibetan plateau. *Chin. J. Geophys.* **2017**, *60*, 2425–2441. [[CrossRef](#)]
53. Jiang, F.; Chen, X.; Unsworth, M.J.; Cai, J.; Han, B.; Wang, L.; Dong, Z.; Cui, T.; Zhan, Y.; Zhao, G.; et al. Mechanism for the Uplift of Gongga Shan in the Southeastern Tibetan Plateau Constrained by 3D Magnetotelluric Data. *Geophys. Res. Lett.* **2022**, *49*, e2021GL097394. [[CrossRef](#)]
54. Li, Y.; Nocquet, J.; Shan, X.; Jian, H. Heterogeneous Interseismic Coupling Along the Xianshuihe-Xiaojiang Fault System, Eastern Tibet. *JGR Solid Earth* **2021**, *126*, e2020JB021187. [[CrossRef](#)]
55. Geng, Y.; Yang, C.; Wang, X.; Ren, L.; Du, L.; Zhou, X. Age of Crystalline Basement in Western Margin of Yangtze Terrane. *Geol. J. China Univ.* **2007**, *13*, 429–441.
56. Harris, R.A.; Day, S.M. Dynamics of Fault Interaction: Parallel Strike-slip Faults. *JGR Solid Earth* **1993**, *98*, 4461–4472. [[CrossRef](#)]
57. Oglesby, D. Rupture Termination and Jump on Parallel Offset Faults. *Bull. Seismol. Soc. Am.* **2008**, *98*, 440–447. [[CrossRef](#)]
58. Kame, N.; Rice, J.R.; Dmowska, R. Effects of Prestress State and Rupture Velocity on Dynamic Fault Branching. *JGR Solid Earth* **2003**, *108*, 2265. [[CrossRef](#)]
59. Harris, R.A. Introduction to Special Section: Stress Triggers, Stress Shadows, and Implications for Seismic Hazard. *J. Geophys. Res.* **1998**, *103*, 24347–24358. [[CrossRef](#)]
60. Bing, Y.; Shinji, T.; Aiming, L. Coulomb Stress Evolution History as Implication on the Pattern of Strong Earthquakes along the Xianshuihe-Xiaojiang Fault System, China. *J. Earth Sci.* **2018**, *29*, 427–440. [[CrossRef](#)]
61. Guifan, C.; Mervin, B.; Demin, L.; Kai, C.; Minxuan, F.; Dun, W. Paleo-Earthquakes along the Zheduotang Fault, Xianshuihe Fault System, Eastern Tibet: Implications for Seismic Hazard Evaluation. *J. Earth Sci.* **2022**, *33*, 1233–1245. [[CrossRef](#)]
62. Hua, Q.; Pei, S.; Yang, Y.; Xue, X.; Li, L.; Li, J.; Liu, H.; Liu, W. The seismogenic mechanism of the Luding Ms 6.8 earthquake revealed from pre-seismic S-wave velocity structure and b-value distribution of the epicenter area. *Chin. J. Geophys.* **2024**, *67*, 1767–1780. [[CrossRef](#)]

Disclaimer/Publisher’s Note: The statements, opinions and data contained in all publications are solely those of the individual author(s) and contributor(s) and not of MDPI and/or the editor(s). MDPI and/or the editor(s) disclaim responsibility for any injury to people or property resulting from any ideas, methods, instructions or products referred to in the content.